Project Link!: Dynamics and Control of In-Flight Wingtip Docking

John R. Cooper[a]
National Institute of Aerospace, Hampton, VA, 23666

Paul M. Rothhaar[b]
NASA Langley Research Center, Hampton, VA, 23681

Project Link! is a NASA-led effort to study the feasibility of multi-aircraft aerial docking systems. In these systems, a group of vehicles physically link to each other during flight to form a larger ensemble vehicle with increased aerodynamic performance and mission utility. This paper presents a dynamic model and control architecture for a system of fixed-wing vehicles with this capability. The dynamic model consists of the 6 degree-of-freedom fixed-wing aircraft equations of motion, a spring-damper-magnet system to represent the linkage force between constituent vehicles, and the NASA-Burnham-Hallock wingtip vortex model to represent the close-proximity aerodynamic interactions between constituents before the linking occurs. The control architecture consists of a guidance algorithm to autonomously drive the constituents towards their linking partners and an inner-loop angular rate controller. A simulation was constructed from the model, and the flight dynamic modes of the linked system were compared to the individual vehicles. Simulation results for both before and after linking are presented.

[a] Research Engineer, Research Department, 100 Exploration Way, Hampton, VA 23666
[b] Aerospace Technologist, Dynamic Systems and Control Branch, 11 Langley Blvd, Hampton, VA 23681, AIAA Member

Nomenclature

r = position vector in ft

R = rotation matrix

B = vehicle body frame

I = inertial frame

x, y, z = Cartesian coordinates associated with a reference frame

u = x-direction component of velocity in B in ft/s

v = y-direction component of velocity in B in ft/s

w = z-direction component of velocity in B in ft/s

ϕ = roll angle in rad

θ = pitch angle in rad

ψ = yaw angle in rad

s = sine

c = cosine

t = tangent

m = mass in slug

F_A = aerodynamic force in lb_f

g = acceleration due to gravity in ft/s^2

F_T = thrust force in lb_f

F_L = linkage force in lb_f

ω = angular velocity in B in rad/s

J = moment of inertia matrix

M_A = aerodynamic moment in ft-lb_f

M_L = linkage moment in ft-lb_f

$\bar{q}$ = dynamic pressure in slug/(ft-s^2)

S = wing area in ft^2

α = angle of attack in rad

C_D = drag coefficient

C_Y = side force coefficient

C_L = lift coefficient

b = wingspan in ft

$\bar{c}$ = average chord length in ft

C_l = roll moment coefficient

C_m = pitch moment coefficient

C_n = yaw moment coefficient

δ = distance vector between two linkage mechanisms in ft

i, j = agent indices

r_L = position of linkage mechanism in B

F_{L_δ} = linkage spring force in lb_f

F_{L_M} = linkage magnetic force in lb_f

K = spring constant in lb_f/ft

C = damping constant in lb_f/(ft/s)

μ = permeability of air in T-ft/A

q = magnetic pole strength in A-ft

K_τ = rotational spring constant in ft-lb_f/rad

C_τ = rotational damping constant in ft-lb_f/(rad/s)

W_{wake} = wake-induced downwash in ft/s

W_r, W_l = wake-induced downwash from right wingtip and left wingtip respectively in ft/s

V_{wake} = wake-induced sidewash in ft/s

V_r, V_l = wake-induced sidewash from right wingtip and left wingtip respectively in ft/s

r_c = vortex core radius in ft

ρ = air density in slug/ft^3

V = free-stream velocity in ft/s

LW = left wingtip

RW = right wingtip

CG = center of gravity

β = sideslip angle in rad

$\tilde{p}$ = non-dimensional roll rate

$\tilde{\omega}$ = non-dimensional angular velocity

D = desired vehicle body frame

r_d = desired position in ft

d, K_d, K_R = guidance parameters

Ψ = error function

e = attitude error

p = x-direction component of ω in B in rad/s

q = y-direction component of ω in B in rad/s

r = z-direction component of ω in B in rad/s

q_{cmd} = command for q in rad/s

r_{cmd} = command for r in rad/s

T = thrust magnitude in lb_f

r_e = position error in ft

$K_{p_{T_V}}$ = proportional speed error gain in lb_f/(ft/s)

$K_{p_{T_r}}$ = proportional position error gain in lb_f/ft

$K_{i_{T_V}}$ = integral speed error gain in lb_f/ft

$K_{i_{T_i}}$ = integral position error gain in lb_f/(ft-s)

$K_{d_{T_V}}$ = derivative speed error gain in lb_f/(ft/s^2)

$K_{d_{T_r}}$ = derivative speed error gain in lb_f/(ft/s)

δ_a = differential aileron deflection in rad

$K_{p_{\delta_a}}$ = proportional roll gain in s

p_{cmd} = command for p in rad/s

$K_{i_{\delta_a}}$ = integral roll gain in s^2

$K_{d_{\delta_a}}$ = derivative roll gain

δ_e = elevator deflection in rad

$K_{p_{\delta_e}}$ = proportional pitch gain in s

$K_{i_{\delta_e}}$ = integral pitch gain in s^2

$K_{d_{\delta_e}}$ = derivative pitch gain

K_{p_z} = proportional altitude gain in rad/ft

K_{i_z} = integral altitude gain in rad/(ft-s)

K_{d_z} = derivative altitude gain rad/(ft/s)

δ_r = rudder deflection in rad

$K_{p_{\delta_r}}$ = proportional pitch gain in s

$K_{i_{\delta_r}}$ = integral pitch gain in s^2

$K_{d_{\delta_r}}$ = derivative pitch gain

δ_{a_R} = right aileron deflection in rad

δ_{a_L} = left aileron deflection in rad

$\hat{\theta}$ = generic nonlinear aerodynamic model parameters

y_{δ_a} = y-distance from CG to ailerons in B in ft

$\tilde{q}$ = non-dimensional pitch rate

$\tilde{r}$ = non-dimensional yaw rate

I. Introduction

Project Link! is a NASA-led effort to study groups of aerial vehicles with the capability of physically linking to each other to form a larger structure with improved aerodynamic performance and mission utility

compared to the individual constituents. This paper investigates dynamics and control for a group of fixed-wing aircraft with this capability and provides simulation results for both the linked and unlinked phases of flight. During the linking phase of flight, an autonomous leader-follower controller is employed such that each vehicle is driven towards the point where its wingtip coincides with its partner vehicle's wingtip. The main contributions of this work are the dynamic models for the individual and linked vehicles and the simulation results for the linking phase and linked flight.

Linked aircraft have the potential to drastically increase the mission capabilities of an aircraft system. Such coordination could enable high altitude, long endurance (HALE) missions with vertical takeoff and landing of component vehicles from unimproved sites. The same system could reconfigure to be capable of a heavy lift mission. Furthermore, in-flight linking allows for multi-leg missions that consist of efficient flight to a remote location followed by a distributed multi-agent leg.

Linked aircraft may find applications in missions such as search and rescue, cartography, reconnaissance, package delivery, and atmospheric satellites. For observational missions, the aircraft would fly to the desired location in an efficient, large fixed-wing mode. Then, the system would break apart into its individual units to cover ground in an optimal distributed way. In a persistent atmospheric satellite mission, units would break off for refueling and immediately be replaced by a new aircraft. In this manner, the ensemble craft could stay airborne indefinitely. Additionally, HALE vehicles have high wing aspect ratios which make them sensitive to atmospheric turbulence. This is what caused the crash of NASA's Helios prototype [1]. A system of linked aircraft would be capable of breaking off into individual agents during turbulence and then re-linking once it is safe to do so.

Flight testing of linked aircraft was first performed in the 1950's by the US Air Force with projects TipTow [2] and Tom-Tom [3]. These projects were carried out in parallel with the objective of increasing the range of fighter planes. Both involved linking the wingtips of the fighters to the wingtips of a larger bomber aircraft. Several successful flights were performed during both projects. However, introducing an autopilot to Project TipTow resulted in a failure which caused the loss of two planes and their crews. Project Tom-Tom was canceled as a result of the link separating during flight due to wingtip vortices, although all

crew members landed safely.

In the intervening years, research has been done on similar ideas such as the multibody transport concept by Moore and Maddalon which consists of two passenger jet fuselages joined together by a wing between them [4]. This design allowed for a lower weight than two individual planes, due to reduced bending moment acting on the common wing and had a lift-to-drag ratio increase of 8-10%. Magill et. al. later studied the effects of wingtip-docked flight. A method for stability analysis was given in [5] and a 20-40% performance increase over individual flight was shown in [6].

With modern day increased capability of unmanned systems and control hardware, there has been renewed interest in this problem. Several researchers have studied modular robotics over the last decade and a half [7–10]. These systems consist of many small, often cube-shaped robots that are capable of arranging themselves in various configurations to complete different tasks. Oung et. al. extended this concept to aerial robots by developing an experimental platform known as the Distributed Flight Array [11]. This array consists of many single rotor aircraft that dock with each other on the ground to form an arbitrarily-shaped multi-rotor vehicle. The individual craft are, however, unstable in solo flight.

More recently, Montalvo and Costello investigated flight dynamic modes for linked fixed-wing aircraft in wingtip-docked, nose-to-tail docked, and lattice configurations [12]. Troub and Montalvo have further analyzed the controllability of these configurations in [13]. Montalvo's dissertation addresses other aspects of the problem including linkage mechanism design and controller design [14].

Under the auspices of Project Link!, Patterson, et. al. considered the conceptual design for a linked vehicle ensemble for a distributed aerial presence or payload mission in [15]. Also as a Project Link! study, Cooper and Rothhaar developed a potential field-based guidance algorithm for in-flight linking of a group of multi-rotor vehicles in [16].

This paper establishes a guidance algorithm for in-flight linking of fixed-wing aircraft. A dynamic model is constructed using the Generic Nonlinear Aerodynamic (GNA) model in [17]. The NASA Burnham-Hallock Model [18] is implemented since wingtip vortex effects are a significant disturbance seen in the close-proximity flight required for wingtip docking. The guidance algorithm developed here is adapted from the virtual leader

path-following algorithm given in [19]. In our case, the virtual leader is replaced with a real leader aircraft, and thus the path-wise speed of the vehicle is not decided by the algorithm, but matches that of the real leader. The linkage forces and moments acting on the vehicles are modeled as a set a spring-damper systems with an additional magnetic force contribution. The simulation results reveal the open-loop dynamic modes of the linked-ensemble, the trajectories and aerodynamic forces during the linked phase, and the dynamic response to doublet commands during linked flight. The paper is organized as follows: Section II develops the dynamic model for the system, Section III presents the wingtip docking guidance algorithm, Section IV defines the inner-loop attitude rate controller for each vehicle, Section V presents the simulation results, and Section VI concludes the paper and discusses future work.

II. Fixed-Wing Aircraft Dynamics

We will adapt a standard rigid body dynamic model from [20] with the addition of forces and moments due to linked vehicles. The translational and rotational kinematic equations of a fixed-wing aircraft are given by

$$\dot{r} = R_B^I \begin{bmatrix} u \\ v \\ w \end{bmatrix} \tag{1}$$

$$\begin{bmatrix} \dot{\phi} \\ \dot{\theta} \\ \dot{\psi} \end{bmatrix} = \begin{bmatrix} 1 & s_\phi t_\theta & c_\phi t_\theta \\ 0 & c_\phi & -s_\phi \\ 0 & s_\phi / c_\theta & c_\phi / c_\theta \end{bmatrix} \omega \tag{2}$$

where r is the position vector in the inertial frame, R_B^I is the rotation matrix from the body frame to inertial frame, $\begin{bmatrix} u & v & w \end{bmatrix}^\top$ is the velocity vector in the body frame, ϕ, θ, and ψ are the roll, pitch, and yaw angles respectively, s, c, and t denote the sine, cosine, and tangent of the subscripted angle respectively, and ω is the body frame angular velocity vector. Note that the body frame, $B\{\vec{x}, \vec{y}, \vec{z}\}$, is defined with the x-axis pointing forward, the z-axis pointing downward, and the body y-axis completing the triad pointing out of

the right wing. The origin of B is located at the vehicle's center of gravity. R_B^I is given in [21] by

$$R_B^I = \begin{bmatrix} c_\theta c_\psi & s_\phi s_\theta c_\psi - c_\phi s_\psi & c_\phi s_\theta c_\psi + s_\phi s_\psi \\ c_\theta s_\psi & s_\phi s_\theta s_\psi + c_\phi c_\psi & c_\phi s_\theta s_\psi - s_\phi c_\psi \\ -s_\theta & s_\phi c_\theta & c_\phi c_\theta \end{bmatrix} \tag{3}$$

The vehicle dynamic equations are given by

$$\begin{bmatrix} \dot{u} \\ \dot{v} \\ \dot{w} \end{bmatrix} = \frac{1}{m} \left[F_A + m R_I^B \begin{bmatrix} 0 \\ 0 \\ g \end{bmatrix} + F_T + F_L \right] - \omega \times \begin{bmatrix} u \\ v \\ w \end{bmatrix} \tag{4}$$

$$\dot{\omega} = I^{-1} \left[M_A + M_L - \omega \times (J\omega) \right] \tag{5}$$

where m is the vehicle mass, F_A is the total aerodynamic force, $R_I^B = R_B^{I\top}$ is the rotation matrix from the body frame to inertial frame, g is the acceleration due to gravity, F_T is the propulsive force on the vehicle, F_L is the force due to linked vehicles, J is the vehicle moment of inertia matrix, M_A is the total aerodynamic moment, and M_L is the moment due to linked vehicles.

The aerodynamic forces and moments are given by

$$F_A = \bar{q} S \begin{bmatrix} -c_\alpha & 0 & s_\alpha \\ 0 & 1 & 0 \\ -s_\alpha & 0 & -c_\alpha \end{bmatrix} \begin{bmatrix} C_D \\ C_Y \\ C_L \end{bmatrix} \tag{6}$$

$$M_A = \bar{q} S \begin{bmatrix} b & 0 & 0 \\ 0 & \bar{c} & 0 \\ 0 & 0 & b \end{bmatrix} \begin{bmatrix} C_l \\ C_m \\ C_n \end{bmatrix} \tag{7}$$

where $\bar{q}$ is the dynamic pressure, S is the planform area of the wing, α is the wing angle of attack, C_D, C_Y, and C_L are the drag, sideforce, and lift coefficients respectively, b is the wingspan, $\bar{c}$ is the chord length, and C_l, C_m, and C_n are the roll, pitch, and yaw moment coefficients. The aerodynamic coefficients are obtained using the generic nonlinear aerodynamic (GNA) model found in [17]. Details of the GNA are provided in the Appendix.

A. Linkage Mechanism Model

The force and moment from the linkage will be represented as a spring-damper system with translational and rotational components. Additionally, we will model magnets at the wingtips which supply an attractive force before the physical link is made. We will consider magnets at each vehicle's wingtips with identical pole strengths. Let the location of the linkage mechanism in the body frame be r_L. Let the distance vector between the two linkage mechanisms on two linked aircraft represented in the body frame of the vehicle we are modeling be

$$\delta = R^B_{I\,i}\left(R^I_{B\,j} r_{L_j} + r_j - R^I_{B\,i} r_{L_i} - r_i\right) \tag{8}$$

where the subscript i denotes the vehicle we are modeling, and the subscript j represents its linked partner. Then $\dot{\delta}$ is given by

$$\dot{\delta} = R^I_{B\,j}\left(\omega_j \times r_{L_j} + \begin{bmatrix} u_j \\ v_j \\ w_j \end{bmatrix}\right) - R^I_{B\,i}\left(\omega_i \times r_{L_i} + R^B_{I\,i}\begin{bmatrix} u_i \\ v_i \\ w_i \end{bmatrix}\right) \tag{9}$$

The translational spring-damper force is

$$F_{L_\delta} = K\delta + C\dot{\delta} \tag{10}$$

where K is the spring constant and C is the damping constant. The magnetic force is given by the inverse square relationship

$$F_{L_M} = \frac{\mu q^2}{4\pi||\delta||^2}\frac{\delta}{||\delta||} \tag{11}$$

where μ is the permeability of air, and q is the magnetic pole strength. $\frac{\delta}{||\delta||}$ is the unit vector in the direction of δ, which specifies the direction of the magnetic force.

The rotational spring component is modeled as a moment that is proportional to the Euler angles that define the rotation from vehicle i's body to vehicle j's body frame. This rotation matrix is

$$R^{B_j}_{B_i} = R^B_{I\,j} R^I_{B\,i} \tag{12}$$

The Euler angles corresponding to $R_{B_i}^{B_j}$ can be solved from (3) as

$$\begin{aligned}\theta_{i,j} &= -\sin^{-1}\left(R_{B_i\,3,1}^{B_j}\right) \\ \phi_{i,j} &= \sin^{-1}\left(\frac{R_{B_i\,3,2}^{B_j}}{\cos\left(\theta_{i,j}\right)}\right) \\ \psi_{i,j} &= \cos^{-1}\left(\frac{R_{B_i\,1,1}^{B_j}}{\cos\left(\theta_{i,j}\right)}\right)\end{aligned} \tag{13}$$

The rotational damping is proportional to angular velocity of vehicle j in vehicle i's body frame. That is

$$\omega_{j/i} = R_{B_j}^{B_i}\omega_j - \omega_i = {R_{B_i}^{B_j}}^{\top}\omega_j - \omega_i \tag{14}$$

The total moment on the vehicle due to the link consists of the rotational spring and damper torque as well as a component resulting from the translational spring-damper force since the linkage mechanism is not located at the vehicle's center of gravity. The total linkage moment, M_L is then given by

$$M_L = -K_\tau \begin{bmatrix}\phi_{i,j} \\ \theta_{i,j} \\ \psi_{i,j}\end{bmatrix} + C_\tau\omega_{j/i} + r_L \times F_L \tag{15}$$

where K_τ is the rotational spring constant and C_τ is the rotational damping constant.

B. Wingtip Vortex Effects

Before the vehicles link, each vehicle experiences an induced velocity caused by the wingtip vortices of the other aircraft in the system. To model this effect, the NASA-Burnham-Hallock Model is used to obtain

a three-dimensional wake velocity field around the wingtips [18]. The model is defined as follows:

$$
\begin{aligned}
W_{wake}(x,y,z) &= -W_r(x,y,z) + W_l(x,y,z) \\
W_r(x,y,z) &= \frac{\Gamma}{4\pi}\frac{y-b/2}{(y-b/2)^2+z^2+r_c^2}\left[1-\frac{x}{\sqrt{x^2+(y-b/2)^2+z^2}}\right] \\
W_l(x,y,z) &= \frac{\Gamma}{4\pi}\frac{y+b/2}{(y+b/2)^2+z^2+r_c^2}\left[1-\frac{x}{\sqrt{x^2+(y+b/2)^2+z^2}}\right] \\
V_{wake}(x,y,z) &= -V_r(x,y,z) + V_l(x,y,z) \\
V_r(x,y,z) &= \frac{\Gamma}{4\pi}\frac{-z}{(y-b/2)^2+z^2+r_c^2}\left[1-\frac{x}{\sqrt{x^2+(y-b/2)^2+z^2}}\right] \\
V_l(x,y,z) &= \frac{\Gamma}{4\pi}\frac{-z}{(y+b/2)^2+z^2+r_c^2}\left[1-\frac{x}{\sqrt{x^2+(y+b/2)^2+z^2}}\right]
\end{aligned} \tag{16}
$$

where W_{wake} and V_{wake} are the wake-induced downwash and sidewash respectively in the body frame of the inducing aircraft, the subscripts r and l denote contributions from the left and right wingtips respectively, x, y, and z are Cartesian coordinates in the same frame, r_c is the core radius of the vortex, and

$$
\Gamma = \frac{4mg}{\rho V \pi b} \tag{17}
$$

where ρ is the air density and V is the free-stream velocity. We will establish an approximation of overall wake-induced velocity experienced by aircraft i as the average of three points along the wingspan. For this calculation, consider points at each wingtip and at the center of gravity of the vehicle. Then the total wake-induced velocity field is given by

$$
\begin{bmatrix} u_{wake} \\ v_{wake} \\ w_{wake} \end{bmatrix} = \sum_{j=1, j\neq i}^{n} R_{B_j}^{B_i} \begin{bmatrix} 0 \\ \frac{V_{wake_j}(x_{LW},y_{LW},z_{LW}) + V_{wake_j}(x_{RW},y_{RW},z_{RW}) + V_{wake_j}(x_{CG},y_{CG},z_{CG})}{3} \\ \frac{W_{wake_j}(x_{LW},y_{LW},z_{LW}) + W_{wake_j}(x_{RW},y_{RW},z_{RW}) + W_{wake_j}(x_{CG},y_{CG},z_{CG})}{3} \end{bmatrix} \tag{18}
$$

where the subscripts LW and RW denote the left and right wingtips respectively, CG denotes the center of gravity, and n is the number of vehicles in the system.

Figure 1 shows a cross-section of the wake velocity field induced by wingtip vortices of a single aircraft according to the NASA-Burnham-Hallock model. Figure 2 shows the resulting velocity field when two vehicles come in close proximity of each other. We can see that the upwash in between the wingtips increases, which results in rolling moments on both vehicles that must be overcome by the inner-loop controllers.

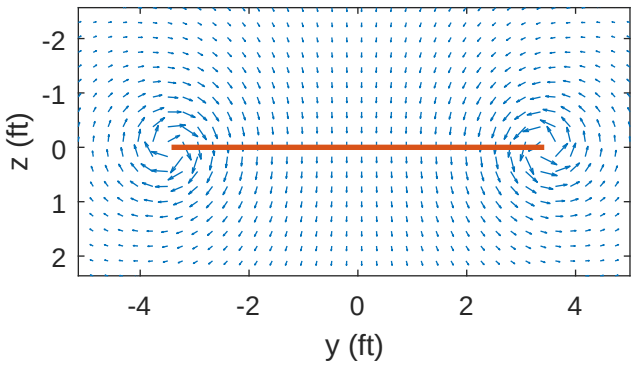

Fig. 1: Cross-section of wake-induced velocity flow field at $x = 0$. The red line represents the wing.

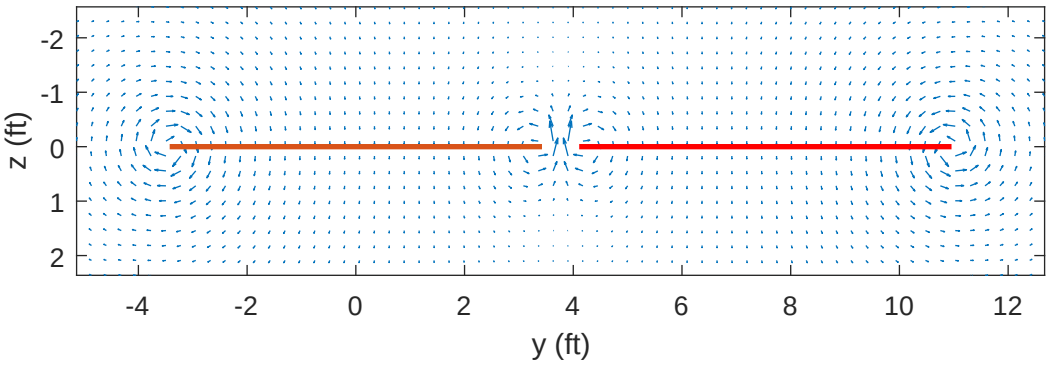

Fig. 2: Cross-section of wake-induced velocity flow field at $x = 0$ for two vehicles in close proximity. The red lines represents the two wings.

The wingtip vortices effect angle-of-attack, α, sideslip angle, β, and non-dimensional roll rate, $\tilde{p}$ of

aircraft i according to

$$\alpha = \tan^{-1}\left(\frac{w - w_{wake}}{u - u_{wake}}\right) \tag{19}$$

$$\beta = \sin^{-1}\left(\frac{v - v_{wake}}{\sqrt{(u - u_{wake})^2 + (v - v_{wake})^2 + (w - w_{wake})^2}}\right) \tag{20}$$

$$\Delta\tilde{p} = \left(\sum_{j=1, j\neq i}^{N} R_{B_j}^{B_i} \begin{Bmatrix} 0 \\ V_{wake_j}(x_{LW}, y_{LW}, z_{LW}) \\ W_{wake_j}(x_{LW}, y_{LW}, z_{LW}) \end{Bmatrix} - \sum_{j=1, j\neq i}^{N} R_{B_j}^{B_i} \begin{bmatrix} 0 \\ V_{wake_j}(x_{RW}, y_{RW}, z_{RW}) \\ W_{wake_j}(x_{RW}, y_{RW}, z_{RW}) \end{bmatrix}\right) \div V \tag{21}$$

The total non-dimensional body axis angular velocity is given by

$$\tilde{\omega} = \frac{1}{2V} \begin{bmatrix} b & 0 & 0 \\ 0 & \bar{c} & 0 \\ 0 & 0 & b \end{bmatrix} \omega + \begin{bmatrix} \Delta\tilde{p} \\ 0 \\ 0 \end{bmatrix} \tag{22}$$

α, β, and $\tilde{\omega}$ are inputs into a aerodynamic model used to obtain the aerodynamic coefficients, C_D, C_Y, C_L, C_l, C_m, C_n.

III. Guidance Algorithm

A guidance algorithm is used to autonomously guide each aircraft towards its mate vehicle. This will be adapted from the virtual leader path-following algorithm in [19].

First, a desired body frame is defined as $D\{\vec{x}_d, \vec{y}_d, \vec{z}_d\}$ with origin coincident with the origin of the actual body frame at the vehicle's center of gravity. Let r_d be the desired aircraft position, which results in the linkage mechanisms of both vehicles coinciding, and let r_L be the position of a vehicle's linkage mechanism in its body frame. Then r_d can be expressed as

$$r_d = r_j + R_{B\,j}^{I} r_{L_j} - R_{B\,i}^{I} r_{L_i} \tag{23}$$

The desired body frame unit vectors are defined by

$$\begin{aligned} \vec{x}_d &= \frac{d\vec{x}_j - (r_{i_y} - r_{d_y})\vec{y}_j - (r_{i_z} - r_{d_z})\vec{z}_j}{\sqrt{d^2 + (r_{i_y} - r_{d_y})^2 + (r_{i_z} - r_{d_z})^2}} \\ \vec{y}_d &= \frac{(r_{i_y} - r_{d_y})\vec{x}_j + d\vec{y}_j}{\sqrt{d^2 + (r_{i_y} - r_{d_y})^2}} \\ \vec{z}_d &= \vec{x}_d \times \vec{y}_d \end{aligned} \tag{24}$$

where d is a parameter which affects how aggressively the aircraft turns towards its mate. The smaller d is, the more aggressive the maneuvers. d is determined as a function of the vehicle position error, $r_d - r_i$. d is updated according to

$$d = K_d||r_d - r_i|| \tag{25}$$

This allows for more aggressive maneuvers to close a small position error, and more benign maneuvers when the distance to the desired position is large.

Let R_B^D be the rotation matrix from the body frame to the desired body frame. When the two frames are aligned, R_B^D is equal to the identity matrix. We can then form an error function, Ψ, using $R_{B\,1,1}^D$ as

$$\Psi = \left(1 - R_{B\,1,1}^D\right) \tag{26}$$

Since $-1 \leq R_{B\,1,1}^D \leq 1$, Ψ is a positive semidefinite function. Also, the only time $\Psi = 0$ is when the body frame and desired body frame are aligned. Thus, the guidance algorithm will be designed such that $\dot{\Psi} \leq 0$.

Differentiating (26) results in

$$\dot{\Psi} = -\dot{R}_{B\,1,1}^D \tag{27}$$

The time derivative of R_B^D is given by

$$\dot{R}_B^D = R_B^D \left(\left\{\omega_{B/D}\right\}_B\right)^\wedge \tag{28}$$

where $\left\{\omega_{B/D}\right\}_D$ is the angular velocity of the desired frame with respect to the body frame expressed in the body frame, and for any vector, $x \in \mathbb{R}^3$, $(x)^\wedge$ denotes the skew-symmetric matrix,

$$(x)^\wedge = \begin{bmatrix} 0 & -x_3 & x_2 \\ x_3 & 0 & -x_1 \\ -x_2 & x_1 & 0 \end{bmatrix} \tag{29}$$

From (28), we can write

$$\dot{R}_{B\,1,1}^D = \begin{bmatrix} R_{B\,1,3}^D & -R_{B\,1,2}^D \end{bmatrix} \begin{bmatrix} 0 & 1 & 0 \\ 0 & 0 & 1 \end{bmatrix} \left\{\omega_{B/D}\right\}_B \tag{30}$$

Next, we define the attitude error,

$$e = \begin{bmatrix} R^D_{B\,1,3} & -R^D_{B\,1,2} \end{bmatrix}^\top \tag{31}$$

The elements of e go to zero, only when Ψ also goes to zero. By substituting (30) and (31) into (27), we can write

$$\dot{\Psi} = e^\top \begin{bmatrix} 0 & 1 & 0 \\ 0 & 0 & 1 \end{bmatrix} \left\{\omega_{B/D}\right\}_B \tag{32}$$

$\left\{\omega_{B/D}\right\}_B$ can be expressed as

$$\left\{\omega_{B_i/D}\right\}_{B_i} = \left\{\omega_{B_i/I}\right\}_{B_i} - R^{B_i}_D \left(R^D_{B_j} \left\{\omega_{B_j/I}\right\}_{B_j} + \left\{\omega_{D/B_j}\right\}_D\right) \tag{33}$$

where $R^B_D = R^{D\,\top}_B$. Note that $\left\{\omega_{B_j/I}\right\}_{B_j} = \omega_j$ from the definition in Section II. Letting $\omega = \begin{bmatrix} p & q & r \end{bmatrix}^\top$ where p is roll rate, q is pitch rate, and r is yaw rate, we can rewrite (32) as

$$\dot{\Psi} = e^\top \left(\begin{bmatrix} q \\ r \end{bmatrix}_i - \begin{bmatrix} 0 & 1 & 0 \\ 0 & 0 & 1 \end{bmatrix} R^{B_i}_D \left(R^D_{B_j}\omega_j + \left\{\omega_{D/B_j}\right\}_D\right) \right) \tag{34}$$

To make $\dot{\Psi}$ negative semidefinite, we choose rate commands as

$$\begin{bmatrix} q_{cmd} \\ r_{cmd} \end{bmatrix} = \begin{bmatrix} 0 & 1 & 0 \\ 0 & 0 & 1 \end{bmatrix} R^{B_i}_D \left(R^D_{B_j}\omega_j + \left\{\omega_{D/B_j}\right\}_D\right) - 2K_R e \tag{35}$$

where q_{cmd} is the commanded pitch rate, r_{cmd} is the commanded yaw rate, and K_R is a positive definite gain matrix. (35) constitutes the guidance algorithm.

A. Convergence

Assuming an inner-loop controller is capable of tracking the commands defined in (35), we can substituting (35) back into (34) with $q = q_{cmd}$ and $r = r_{cmd}$. This results in

$$\dot{\Psi} = -2K_R e^\top e \tag{36}$$

Since $e^\top e$ is positive semidefinite, $\dot{\Psi}$ is thus negative semidefinite, which means the error function, Ψ is always driven towards zero by the guidance law given in (35). Furthermore, Ψ reaches steady state when the attitude error, e is the zero vector. Since Ψ is decrescent, the magnitude of e must also be decrescent. Thus, (35) ensures that the vehicle body frame always rotates towards the desired body frame.

IV. Inner-Loop Controller

Thrust is used to match the mating vehicles' velocities and longitudinal separation. Assume that the vehicle thrust vector is aligned with the body x-axis. Then we have $F_T = \begin{bmatrix} T & 0 & 0 \end{bmatrix}^\top$, where T is the thrust magnitude. The position error between the two vehicles is given by

$$r_e = R_I^{B_i} \left(r_j - r_i \right) \tag{37}$$

and the longitudinal separation is the first element of r_e, r_{e_1}. A proportional-integral-derivative (PID) controller is implemented with error signals for both speed and longitudinal separation as

$$T = K_{p_{T_V}} \left(V_j - V_i \right) K_{p_{T_r}} r_{e_1} + K_{i_{T_V}} \int_0^t \left(V_j - V_i \right) d\tau + K_{i_{T_r}} \int_0^t r_{e_1} d\tau + K_{d_{T_V}} \frac{d}{dt} \left(V_j - V_i \right) + K_{d_{T_r}} \frac{dr_{e_1}}{dt} \tag{38}$$

where $K_{p_{T_V}}$, $K_{i_{T_V}}$, and $K_{d_{T_V}}$ are the proportional, integral, and derivative gains respectively on the speed error and $K_{p_{T_r}}$, $K_{i_{T_r}}$, and $K_{d_{T_r}}$ are the proportional, integral, and derivative gains respectively on the longitudinal separation.

Attitude is controlled via the following control surfaces: a pair of differentially moving ailerons for roll, elevator for pitch, and rudder for yaw. A PID controller is implemented for each rotational axis to generate the desired control surface deflection. The elevator is additionally affected by a PID controller on the z-position error between the mating vehicles. This provides additional robustness to the guidance algorithm in Section III. The inner-loop controllers are given as

$$\delta_a = K_{p_{\delta_a}} (p_{cmd} - p) + K_{i_{\delta_a}} \int_0^t (p_{cmd} - p) d\tau + K_{d_{\delta_a}} \frac{d}{dt} (p_{cmd} - p) \tag{39}$$

$$\begin{aligned} \delta_e = {} & K_{p_{\delta_e}} (q_{cmd} - q) + K_{i_{\delta_e}} \int_0^t (q_{cmd} - q) d\tau + K_{d_{\delta_e}} \frac{d}{dt} (q_{cmd} - q) \\ & + K_{p_z} (r_{j_z} - r_{i_z}) + K_{i_z} \int_0^t (r_{j_z} - r_{i_z}) d\tau + K_{d_z} \frac{d}{dt} (r_{j_z} - r_{i_z}) \end{aligned} \tag{40}$$

$$\delta_r = K_{p_{\delta_r}} (r_{cmd} - r) + K_{i_{\delta_r}} \int_0^t (r_{cmd} - r) d\tau + K_{d_{\delta_r}} \frac{d}{dt} (r_{cmd} - r) \tag{41}$$

where δ_a, δ_e, and δ_r are the aileron, elevator, and rudder deflections respectively, $K_{p_{\delta_a}}$, $K_{i_{\delta_a}}$, and $K_{d_{\delta_a}}$ are the are the proportional, integral, and derivative gains respectively on the roll angle error, $K_{p_{\delta_e}}$, $K_{i_{\delta_e}}$, and $K_{d_{\delta_e}}$ are the are the proportional, integral, and derivative gains respectively on the pitch angle error, K_{p_z},

Table 1: GTM properties

Parameter	m	J	b	$\bar{c}$	S
Value	49.6 lb_m	$\begin{bmatrix} 1.327 & 0 & 0.120 \\ 0 & 4.254 & 0 \\ 0.120 & 0 & 5.454 \end{bmatrix}$ slug ft^2	6.849 ft	0.915 ft	5.902 ft

Table 2: Linkage parameters

Parameter	K	C	K_τ	C_τ	μ	q
Value	100 lb_f/ft	62 lb_f/(ft/s)	100 ft-lb_f/rad	62 ft-lb_f/(rad/s)	4.12 $\times 10^{-}6$ T-ft/A	26.2 A-ft

K_{i_z}, and K_{d_z} are the proportional, integral, and derivative gains respectively on the z-position error, and $K_{p_{\delta_r}}$, $K_{i_{\delta_r}}$, and $K_{d_{\delta_r}}$ are the are the proportional, integral, and derivative gains respectively on the yaw angle error.

A. Control Allocation During Linked Flight

When a group of vehicles is linked, the ensemble vehicle becomes over-actuated in the sense that the three angular rates are then controlled by $4n$ control surfaces, where n is the number of vehicles in the ensemble. This allows freedom for the optimization of some criteria in the control allocation. For the purposes of this paper, a simple linked allocation scheme of the outboard-most ailerons for roll, all elevators for pitch, and all rudders for yaw will be utilized. However, we note that optimization of the bending moment at the point of linkage is an interesting problem for future work.

V. Simulation

A simulation was performed for three fixed-wing vehicles. The dynamic model for each vehicle represents the NASA Generic Transport Model (GTM). The GTM properties are given in Table 1, and the linkage mechanism parameters are shown in Table 2.

All three vehicles were trimmed for straight and level flight at 1200 ft altitude. All lateral parameters

Table 3: Trim values

State	**Trim Value**	**Input**	**Trim Value**
u	124.6 ft/s	T	4.119 lb_f
w	10.72 ft/s	δ_e	0.0165 rad
θ	0.0858 rad		

were trimmed to zero, and the longitudinal parameters were trimmed according to Table 3.

A. Flight Dynamic Modes

The linked aircraft model was linearized about the trim point using the MATLAB/Simulink Control Design Toolbox for a single vehicle, two, and three linked vehicles. The poles associated with each of the flight dynamic modes are shown in the complex plane in Figure 3. Note that there exist several higher frequency modes associated with the spring and damper states. Those modes have been omitted from this plot in order to focus on the traditional flight dynamic modes.

It is noted that the short period and phugoid modes are unaffected by adding wingtip-docked vehicles since the longitudinal dynamics remain identical. Only the lateral dynamics are altered.

We can see that the roll mode slows down when more vehicles are added. Typically, an increase in span results in a faster roll mode. However in the case of this linked aircraft system, the roll inertia of the linked configuration is drastically increased. This effect dominates the locus of the roll mode pole in the complex plane. It is also noteworthy that the pole moves much further when going from 1 to 2 vehicles versus going from 2 to 3 vehicles. This implies that as more vehicles are added, the effects of adding span versus adding inertia cancel each other out. Furthermore, the flight dynamics of a two-vehicle ensemble are not very different than those of a three-vehicle ensemble. This means a single roll controller can be used for any ensemble composed of wingtip-docked identical vehicles.

The spiral mode moves similarly to the roll mode, however, this pole becomes unstable. The unstable spiral mode of the linked configuration is very close to the imaginary axis, which is easily stabilized with feedback control. These results are in accordance with previous literature [12].

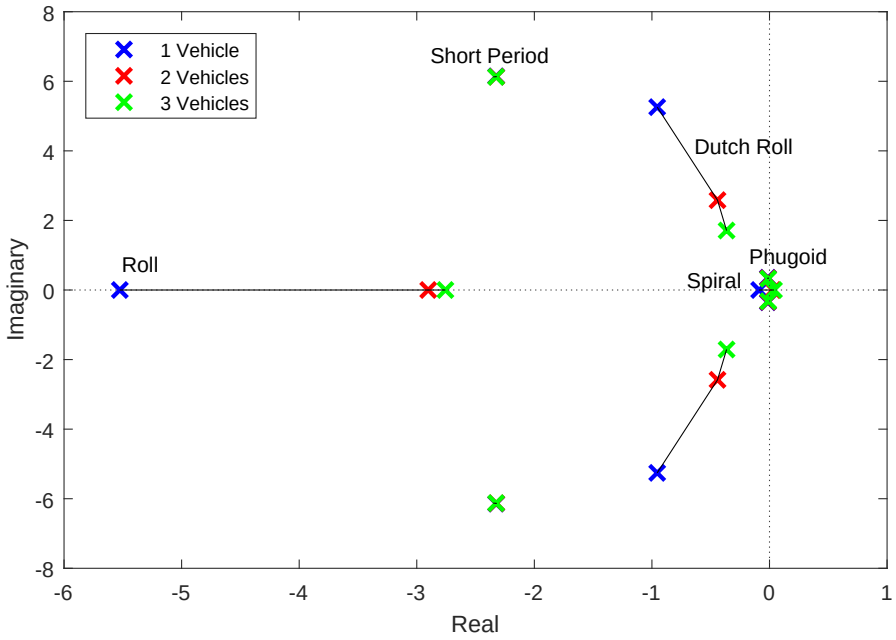

(a) All flight dynamic modes

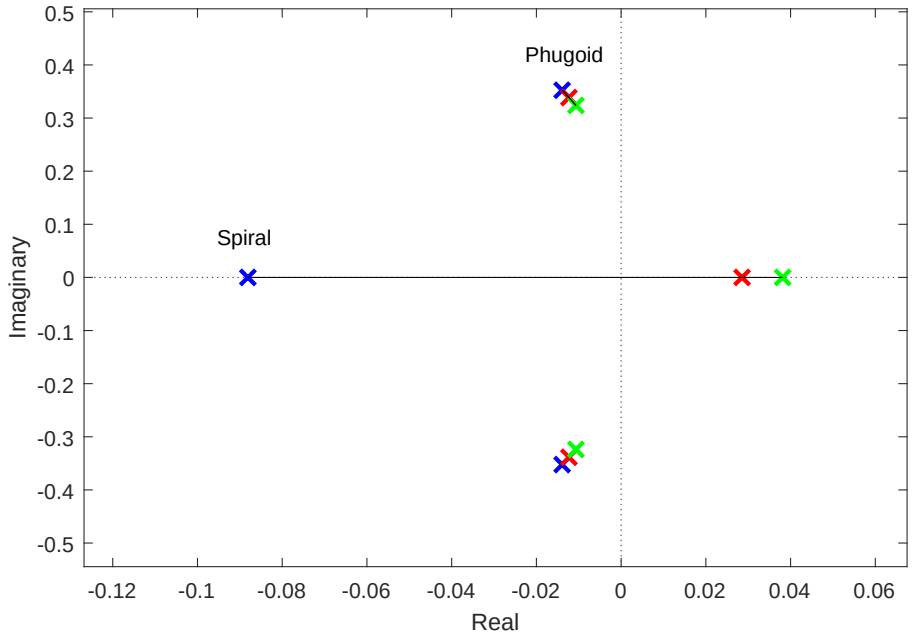

(b) Phugoid and spiral modes

Fig. 3: Flight dynamic modes for one vehicle and two and three linked vehicles

Table 4: Inner-Loop Control Parameters

	Speed	**Longitudinal Separation**	**Roll Rate**	**Pitch Rate**	**Yaw Rate**	**Altitude**
Proportional Gain	10	10	10	10	10	10
Integral Gain	10	10	1	1	1	1
Derivative Gain	10	10	0	0	0	1

B. Linking Phase

The three vehicles were initialized with a lateral separation of 20 ft and no longitudinal separation. The vehicle in the middle of the initial formation served as the mothership. The two vehicles on either side of the mothership were autonomously guided toward it via the guidance algorithm of Section III. The vehicles were considered linked when the distance between wingtips became less than or equal to 0.15 ft. The guidance algorithm parameters were $K_d = 20$ and $K_R = \begin{bmatrix} 0.1 & 0 \\ 0 & 0.1 \end{bmatrix}$. The inner-loop control parameters are shown in Table 4.

Figure 4 shows the trajectories of the centers of mass of the three vehicles during the linking phase. Note that the majority of motion is in the x-axis, thus the x-axis is scaled by $1/50$ so that the motion in all three axes is visible. Vehicle 2 is the mothership, and Vehicles 1 and 3 are the followers. The stars on the plot denote the locations where wingtips became linked.

It can be seen in Figure 4 that the two follower vehicles initially lose altitude as they turn in towards the mothership. This is due to the buildup of sideslip as they maneuver via a yaw rate. The altitude is regained as the wingtips close in on linking and the sideslip is eliminated by realigning their body axes with the mothership's. The altitude hold portion of the inner-loop controllers also plays a role in restoring altitude. Once the vehicles are linked, the altitude hold portion of the inner-loop is switched off, and the wingtip vortex effects go to zero. As the wingtips come together, a transient aerodynamic force is generated by flying through the wake vortex of the neighboring vehicle. This results in the ensemble vehicle experiencing a slight altitude climb after linking.

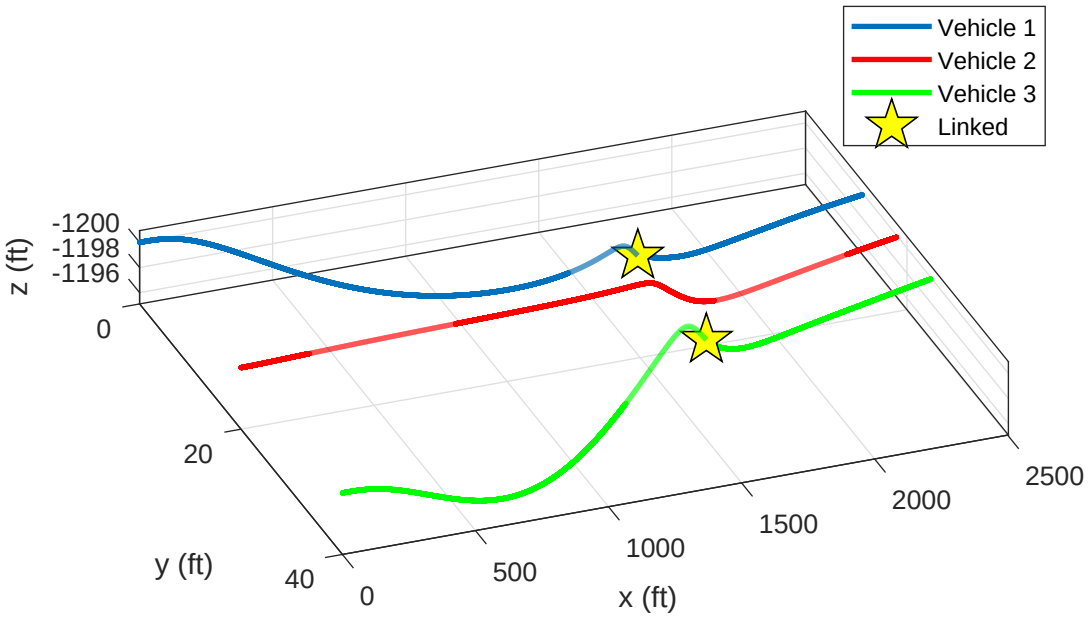

Fig. 4: Vehicle trajectories during the linking phase

Figure 5 shows the aerodynamic forces and moments on each vehicle during the linking phase. As the vehicle wingtips approach the linkage point, the maneuvers they undergo become more aggressive as a result of definition of d in (25). Oscillations are also present because each vehicle is moving through the wake vortices of the other two. The forces and moments seen in this simulation can help drive structural design requirements for linking aircraft.

C. Linked Flight Phase

Figure 6 shows the response of the linked ensemble to a series of attitude rate doublet commands. Rate tracking, Euler angles, and control surface deflections are shown. Note that the differential aileron deflection plot shows the total differential aileron deflection for the ensemble. As described in Section IV A, only the

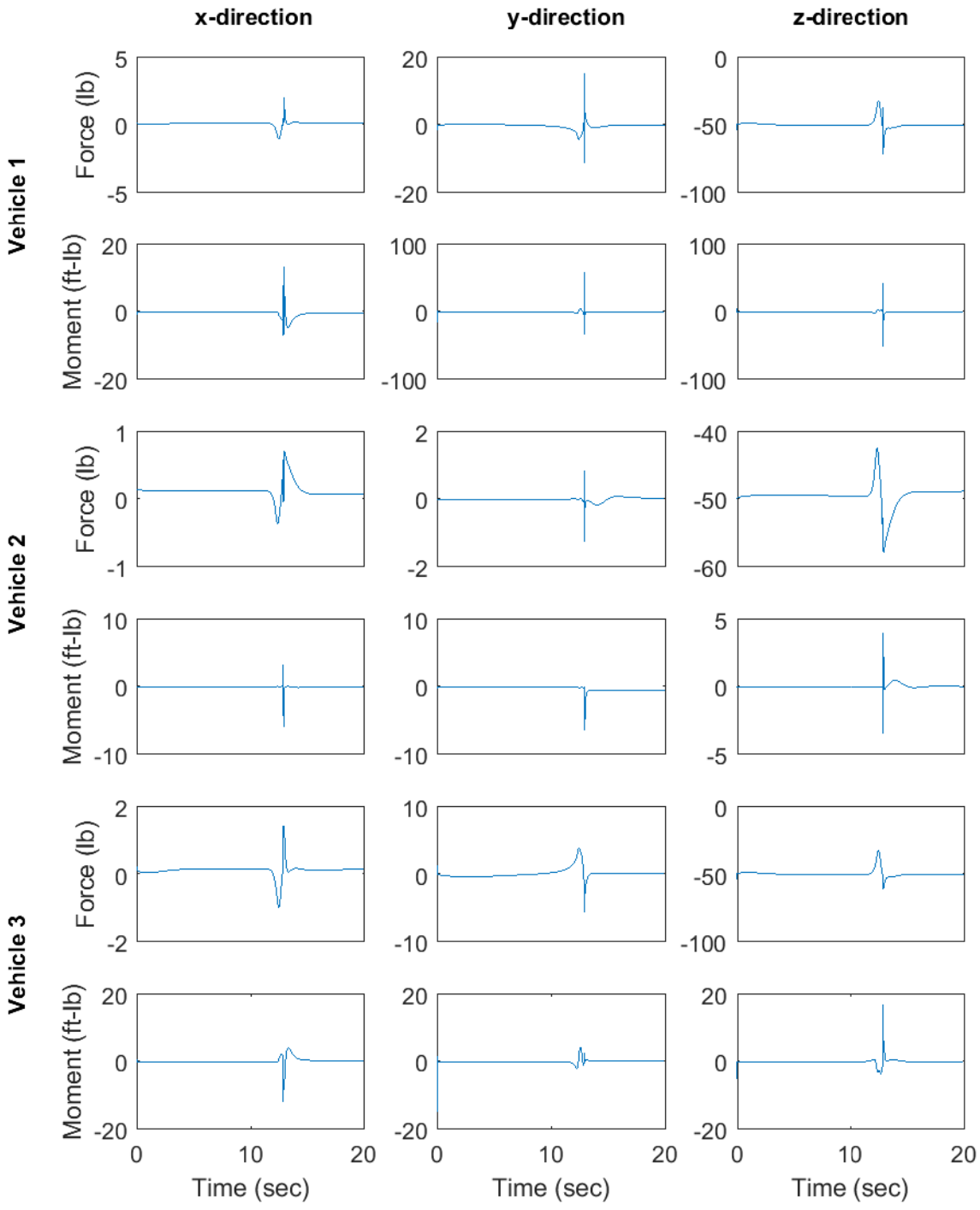

Fig. 5: Aerodynamic forces and moments during the linking phase

outboard-most ailerons are used to control roll. Therefore the signal shown in Figure 6 is

$$\delta_a = \delta_{a_R 3} - \delta_{a_L 1} \tag{42}$$

We note that in all three axes, all three constituent vehicles are able to track the commanded rates, and most importantly, the responses of all constituent vehicles are very similar. This means that the linked ensemble is behaving as a single vehicle. While the inertia about the pitch axis increases threefold when the vehicles are linked, the ensemble vehicle has three times the control power of the individual constituents. Thus the closed-loop pitch dynamics of the ensemble vehicle are the same as that for the constituents. This is why the pitch rate tracking is much tighter than the roll and yaw rate tracking. It is also worth noting that actuator dynamics are not included in this simulation. Therefore, the fast response of the control surfaces shown in Figure 6 may not be achievable in a real system. We leave the inclusion of actuator dynamics as a possible future path for increasing the fidelity of these methods.

As the linked ensemble rolls, the y and z-positions of Vehicles 1 and 3 rise and sink. Figure 7 shows the differences between the outboard constituent vehicle y and z-positions and the mothership y and z-position during the doublet maneuvers. These distances are measured in a coordinate frame with y and z-axes aligned with the inertial frame, and x-axis aligned with Vehicle 2's body frame. In other words, the inertial measurements are rotated about the inertial z-axis by ψ_2. The y-distances change very little as a result of the rolling maneuver from 5-10 seconds because they depend on the cosine of a relatively small angle (13° from Figure 6). The change in y-distance is apparent for Vehicle 1 in Figure 7, but this effect for Vehicle 2 is dominated by the linkage dynamics. In contrast, the changes in z-positions are obvious for both vehicles. Vehicle 1 ascends by about 1.5 ft while Vehicle 2 descends by the same amount. Figure 7 also shows the changes in z-position that results from the roll-yaw coupling during the yaw doublet from 25-30 seconds.

Figure 8 shows the aerodynamic forces and moments on the linked vehicle as well as the forces and moments from the linkages experienced during the doublet maneuvers. It is shown that all three constituents experience approximately the same aerodynamic forces and moments. The linkage forces and moments result from the fact that the outboard constituents pull on the mothership for roll control of the ensemble since only the most outboard ailerons of the total system are utilized. The largest linkage force experienced is

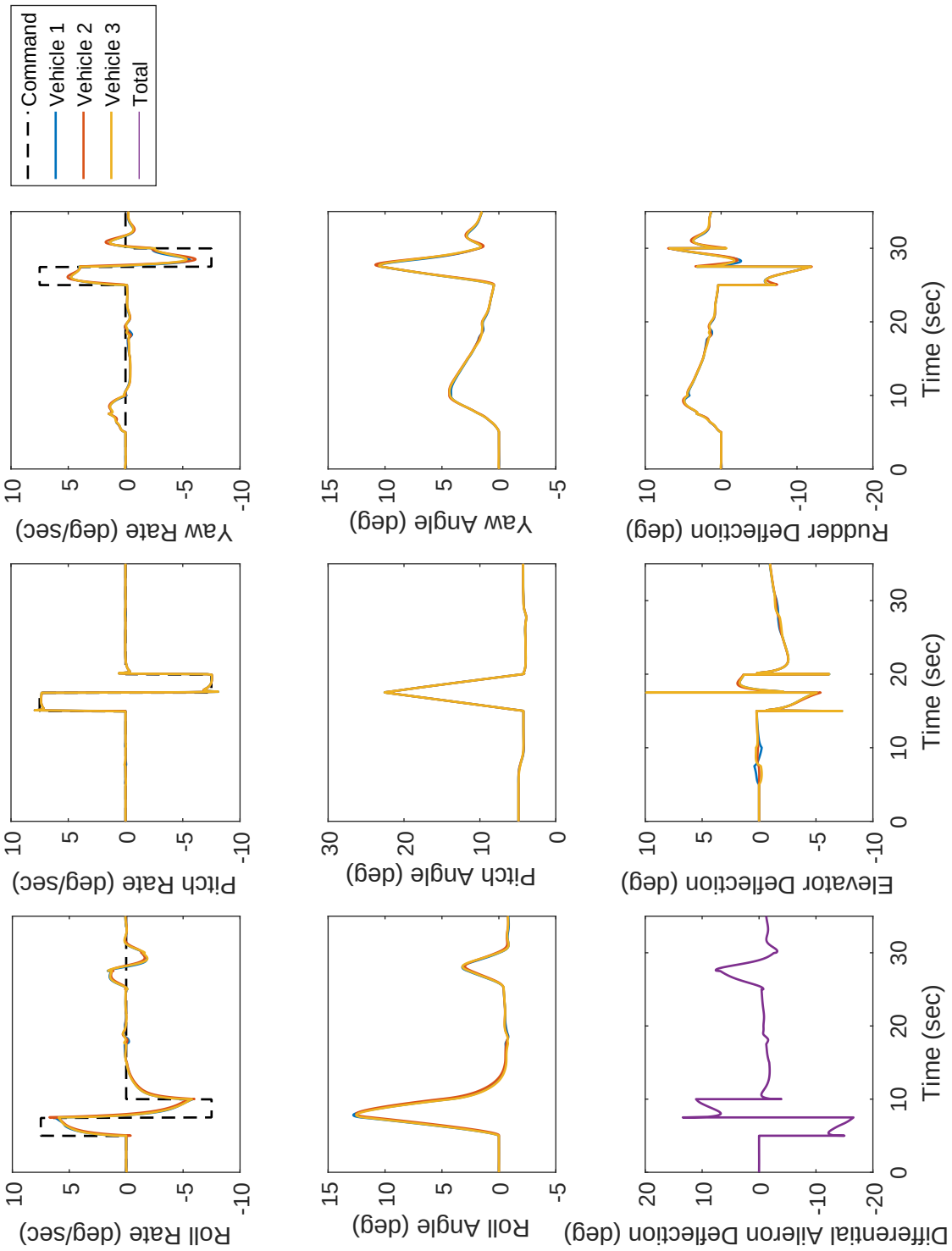

Fig. 6: Doublet response of linked vehicle

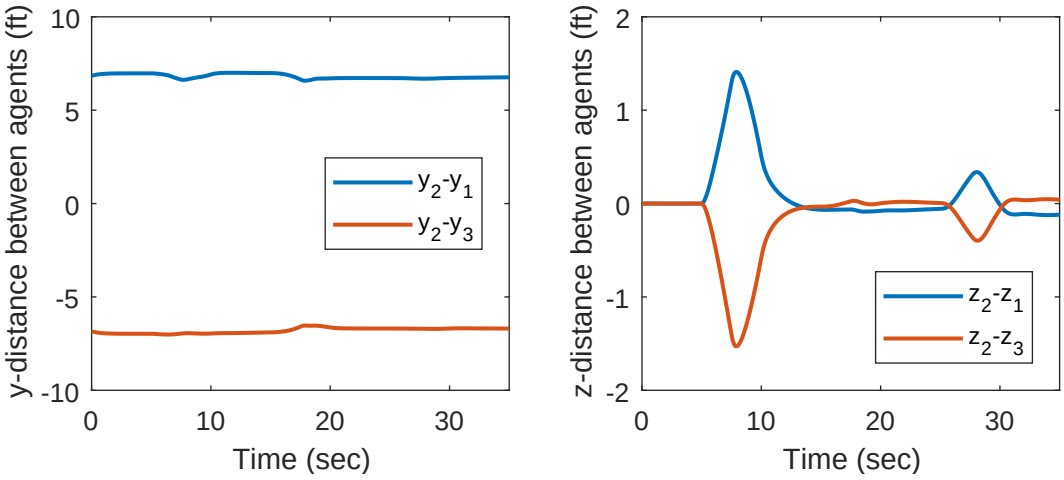

Fig. 7: Difference in y and $z-$positions of the outboard constituents and the mothership

approximately 7 lb, and the largest linkage moment is approximately 20 ft-lb. This simulation data could be used to drive the linkage mechanism design requirements. The model presented here does not account for the weight of the linkage mechanism itself, which would presumably scale with the load it must carry. A 7 lb force constitutes approximately 14% of the vehicle weight. This is a reasonable load to design to, but it remains to be seen how this number would scale to larger aircraft. It is expected that there is some upper bound on vehicle weight for which the linkage load becomes unfeasible to design a mechanism for. Therefore, the set of missions that can most readily benefit from linked aircraft systems are those where the constituent vehicles can be small and light.

VI. Conclusions and Future Work

This paper has presented an approach to dynamic modeling, guidance, and control for in-flight wingtip docking of a group of fixed-wing aircraft. The NASA-Burnham-Hallock model for wingtip vortices was introduced to a generic fixed-wing rigid body aerodynamic model to capture the close-proximity aerodynamic interactions between vehicles in the group. A spring-damper-magnet model was introduced to describe the forces exerted as a result of linked flight. An autonomous guidance algorithm and inner-loop control were developed so that the constituent vehicles behave in a leader-follower manner during the unlinked phase of flight. These models were implemented in a simulation representing NASA's GTM aircraft, and the resulting

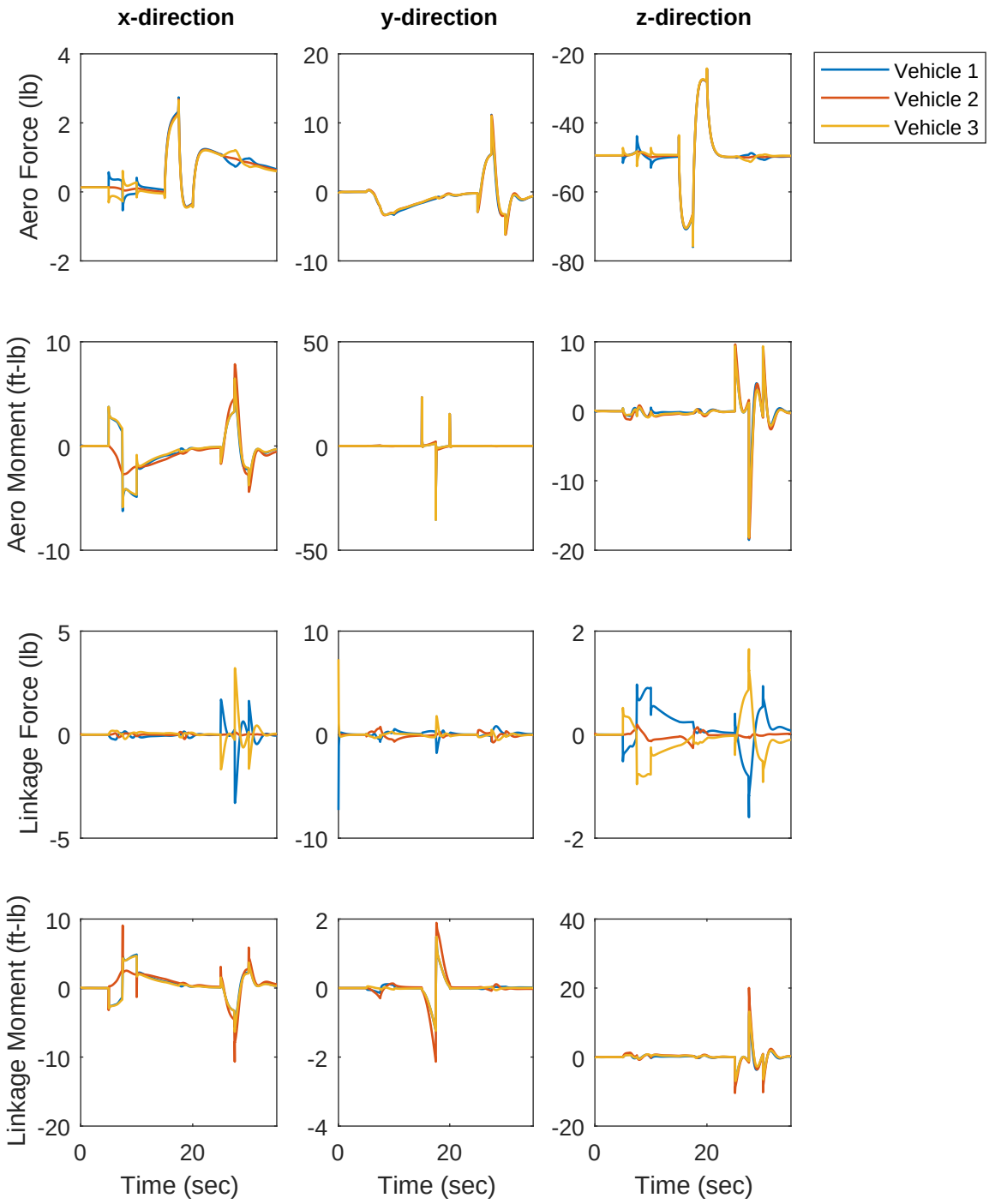

Fig. 8: Aerodynamic and linkage forces and moments on the linked vehicle during doublet maneuvers

linearized dynamic modes were identified for the constituent vehicles as well as a linked ensemble consisting of two and three constituents. Dynamic simulations were performed for both the unlinked and linked phases of flight.

The modeling presented in this paper, while appropriate for the exploratory nature of this work, is admittedly low fidelity. Future work would seek to more accurately characterize the close-proximity aerodynamic interactions between vehicles via wind tunnel experiments or computational fluid dynamic analysis. Similarly, a higher fidelity linkage model could be developed based on a detailed mechanism design. Finally, future modeling efforts would seek to describe an aircraft concept built specifically for a linked flight mission, such as the vehicle described in [15]. This concept is a vertical takeoff and landing vehicle, and thus the model (and control system) would need to be extended to the hover and transition flight regimes.

Another goal for future work is to implement the algorithms presented here in actual flight hardware. This requires an investigation into the necessary sensors, communication, and state estimation schemes such that the constituent vehicles have access to the appropriate feedback signals. Some examples of sensors that will be investigated are GPS, computer vision [22, 23], LIDAR [24], and ultra-wideband radios for close-range localization of member vehicles [25]. Another aspect of implementation that must be addressed is the design of a linking mechanism that can be outfitted onboard the vehicles and the switching of control allocation amongst the various control surfaces under ensemble flight.

Appendix

The GNA model is given by

$$
\begin{aligned}
C_D &= \hat{\theta}_1 + \hat{\theta}_2\alpha + \hat{\theta}_3\alpha\tilde{q} + \hat{\theta}_4\alpha\delta_e + \hat{\theta}_5\alpha^2 + \hat{\theta}_6\alpha^2\tilde{q} + \hat{\theta}_7\alpha^2\delta_e + \hat{\theta}_8\alpha^3 + \hat{\theta}_9\alpha^3\tilde{q} + \hat{\theta}_{10}\alpha^4 - \frac{b}{2y_{\delta_a}}\hat{\theta}_{42}\left(\delta_{a_R} + \delta_{a_L}\right) \\
C_Y &= \hat{\theta}_{11}\beta + \hat{\theta}_{12}\tilde{p} + \hat{\theta}_{13}\tilde{r} + \hat{\theta}_{14}\delta_a + \hat{\theta}_{15}\delta_r \\
C_L &= \hat{\theta}_{16} + \hat{\theta}_{17}\alpha + \hat{\theta}_{18}\tilde{q} + \hat{\theta}_{19}\delta_e + \hat{\theta}_{20}\alpha\tilde{q} + \hat{\theta}_{21}\alpha^2 + \hat{\theta}_{22}\alpha^3 + \hat{\theta}_{24}\alpha^4 - \frac{b}{2y_{\delta_a}}\hat{\theta}_{27}\left(\delta_{a_R} + \delta_{a_L}\right) \\
C_l &= \hat{\theta}_{24}\beta + \hat{\theta}_{25}\tilde{p} + \hat{\theta}_{26}\tilde{r} + \frac{1}{2}\theta_{27}\delta_{a_R} - \frac{1}{2}\hat{\theta}_{27}\delta_{a_L} + \hat{\theta}_{28}\delta_r \\
C_m &= \hat{\theta}_{29} + \hat{\theta}_{30}\alpha + \hat{\theta}_{31}\tilde{q} + \hat{\theta}_{32}\delta_e + \hat{\theta}_{33}\alpha\tilde{q} + \hat{\theta}_{34}\alpha^2\tilde{q} + \hat{\theta}_{35}\alpha^2\delta_e + \hat{\theta}_{36}\alpha^3\tilde{q} + \hat{\theta}_{37}\alpha^3\delta_e + \hat{\theta}_{38}\alpha^4 \\
C_n &= \hat{\theta}_{39}\beta + \hat{\theta}_{40}\tilde{p} + \hat{\theta}_{41}\tilde{r} + \frac{1}{2}\theta_{42}\delta_{a_R} - \frac{1}{2}\hat{\theta}_{42}\delta_{a_L} + \hat{\theta}_{43}\delta_r + \hat{\theta}_{44}\beta^2 + \hat{\theta}_{45}\beta^3
\end{aligned}
\tag{43}
$$

Table 5: GNA parameters

Element of $\hat{\theta}$	**Value**	**Element of $\hat{\theta}$**	**Value**	**Element of $\hat{\theta}$**	**Value**
1	0.019	2	-0.078	3	-27.420
4	0.293	5	3.420	6	288.200
7	-0.040	8	1.819	9	-355.300
10	-6.563	11	-1.003	12	0.033
13	0.952	14	-0.009	15	0.253
16	0.0160	17	15.343	18	30.780
19	0.396	20	12.030	21	0.506
22	-36.300	23	46.130	24	-0.109
25	-0.366	26	0.061	27	-0.079
28	0.021	29	0.182	30	-1.782
31	-44.340	32	-1.785	33	374.000
34	-1748.000	35	2.439	36	1949.000
37	-0.0380	38	0.803	39	0.2031
40	-0.220	41	-0.405	42	-0.009
43	-0.129	44	0	45	0.0064

where $\hat{\theta}$ are the model parameters and y_{δ_a} is the y-distance from the vehicle CG to the center of each aileron, and $\tilde{q}$ and $\tilde{r}$ are the non-dimensional pitch and yaw rates respectively. Note that the GNA has been slightly modified from its presentation in [17] to account for effects of individual aileron deflections. This is a necessary modification to model the linked control allocation described in Section IV A. The GNA parameters are given in Table 5.

[1] Noll, T. E., Brown, J. M., Perez-Davis, M. E., Ishmael, S. D., Tiffany, G. C., and Gaier, M., "Investigation of the Helios Prototype Aircraft Mishap," Mishap report, NASA, 2004.

[2] Anderson, C., "Dangerous Experiments: Wingtip Coupling at 15,000 Feet," *Flight Journal*, Vol. 5, No. 6, 2000, pp. 64.

[3] Miller, J., "Project 'Tom-Tom'," *Aerophile*, Vol. 1, 1977, pp. 161–164.

[4] Moore, J. and Maddalon, D., "Multibody transport concept," *International Very Large Vehicles Conference, 2nd*, No. 19820048448, American Institute of Aeronautics and Astronautics, May 1982, p. 13.

[5] Magill, S. A. and Durham, W. C., "Modelling and Simulation of Wingtip-Docked Flight," *moment*, Vol. 1000, 2002, pp. 2.

[6] Magill, S. A., Schetz, J. A., and Mason, W. H., "Compound Aircraft Transport: A Comparison of Wing Tip-Docked and Close-Formation Flight," *41st Aerospace Sciences Meeting and Exhibit*, 2003, pp. 2003–0607.

[7] Casal, A. and Yim, M. H., "Self-reconfiguration planning for a class of modular robots," *Photonics East'99*, International Society for Optics and Photonics, 1999, pp. 246–257.

[8] Yim, M., Zhang, Y., and Duff, D., "Modular robots," *Spectrum, IEEE*, Vol. 39, No. 2, 2002, pp. 30–34.

[9] Vassilvitskii, S., Yim, M., and Suh, J., "A complete, local and parallel reconfiguration algorithm for cube style modular robots," *Robotics and Automation, 2002. Proceedings. ICRA'02. IEEE International Conference on*, Vol. 1, IEEE, 2002, pp. 117–122.

[10] White, P., Zykov, V., Bongard, J. C., and Lipson, H., "Three Dimensional Stochastic Reconfiguration of Modular Robots." *Robotics: Science and Systems*, Cambridge, 2005, pp. 161–168.

[11] Oung, R. and D'Andrea, R., "The distributed flight array," *Mechatronics*, Vol. 21, No. 6, 2011, pp. 908–917.

[12] Montalvo, C. and Costello, M., "Meta Aircraft Flight Dynamics," *Journal of Aircraft*, Vol. 52, No. 1, 2014, pp. 107–115.

[13] Troub, B. and Montalvo, C., "Meta Aircraft Controllability," *AIAA Atmospheric Flight Mechanics Conference*, 2016, p. 3395.

[14] Montalvo, C., "Meta aircraft flight dynamics and controls," 2014.

[15] Patterson, M. D., Quinlan, J. R., Fredericks, W. J., Tse, E., and Bakhle, I., "A Modular Unmanned Aerial System For Missions Requiring Distributed Aerial Presence or Payload Delivery," *55th AIAA Aerospace Sciences Meeting*, 2017, p. 0210.

[16] Cooper, J. R. and Rothhaar, P. M., "Link!: Potential Field Guidance Algorithm for In-Flight Linking of Multi-Rotor Aircraft," *17th AIAA Aviation Technology, Integration, and Operations Conference*, 2017, p. 3604.

[17] Grauer, J. A. and Morelli, E. A., "A Generic Nonlinear Aerodynamic Model for Aircraft," .

[18] Binetti, P., Ariyur, K. B., Krstic, M., and Bernelli, F., "Formation flight optimization using extremum seeking feedback," *Journal of Guidance, Control, and Dynamics*, Vol. 26, No. 1, 2003, pp. 132–142.

[19] Cichella, V., Xargay, E., Dobrokhodov, V., Kaminer, I., Pascoal, A. M., and Hovakimyan, N., "Geometric 3D path-following control for a fixed-wing UAV on SO (3)," *AIAA Conference of Guidance, Navigation and Control conference*, 2011.

[20] Etkin, B., *Dynamics of atmospheric flight*, Courier Corporation, 2012.

[21] Stevens, B. L., Lewis, F. L., and Johnson, E. N., *Aircraft Control and Simulation: Dynamics, Controls Design, and Autonomous Systems*, John Wiley & Sons, 2015.

[22] Forster, C., Pizzoli, M., and Scaramuzza, D., "SVO: Fast semi-direct monocular visual odometry," *Robotics and Automation (ICRA), 2014 IEEE International Conference on*, IEEE, 2014, pp. 15–22.

[23] Rodríguez-Canosa, G. R., Thomas, S., del Cerro, J., Barrientos, A., and MacDonald, B., "A real-time method to detect and track moving objects (DATMO) from unmanned aerial vehicles (UAVs) using a single camera," *Remote Sensing*, Vol. 4, No. 4, 2012, pp. 1090–1111.

[24] Russ, M., Vohla, M., Stütz, P., and OYoung, S., "LIDAR-based object detection on small UAV: Integration, Experimentation and Results," *AIAA Infotech Conference*, 2012.

[25] Gezici, S., Tian, Z., Giannakis, G. B., Kobayashi, H., Molisch, A. F., Poor, H. V., and Sahinoglu, Z., "Localization via ultra-wideband radios: a look at positioning aspects for future sensor networks," *Signal Processing Magazine, IEEE*, Vol. 22, No. 4, 2005, pp. 70–84.